RESEARCH PAPER

Computing flow, combustion, heat transfer and thrust in a micro-rocket via hierarchical problem decomposition

Marina Campolo · Michele Andreoli ·
Alfredo Soldati

Abstract This work describes the methodology developed to optimize the design of the combustion chamber, the thrust generating nozzle and the cooling system of a micro-rocket using numerical simulations. The coupling between combustion, subsonic/sonic/supersonic flow transition and heat transfer inside the micro-rocket is analysed using a problem decomposition strategy and state-of-the-art numerical techniques. First, the design of the thrust-generating nozzle is optimized; then, the mixing performances and the combustion efficiency are evaluated; finally, the design of the cooling system is verified calculating the heat transfer from the hot gases to the solid shell and to the cooling fluid. Results show that sub-optimal micro-rocket design alternatives can be easily identified through self-validated numerical analyses. In this way, the number of time consuming and costly experiments required for prototypes qualification in the lab can be reduced, focusing the tests on the limited set of sub-optimal alternatives identified by numerical simulations, thus speeding up the development of new devices.

M. Campolo (✉) · M. Andreoli · A. Soldati
Centro Interdipartimentale di Fluidodinamica e Idraulica,
University of Udine, 33100 Udine, Italy
e-mail: marina.campolo@uniud.it

A. Soldati
Dipartimento di Energetica e Macchine, Università di Udine,
33100 Udine, Italy

A. Soldati
CISM, Centro Internazionale di Scienze Meccaniche,
33100 Udine, Italy

1 Introduction

Micro-rocket arrays are increasingly used in aerospace applications as micro-thrusters for the point positioning of small satellites. The main advantage they offer is that the chemical energy stored on-board as fuel can be converted efficiently (and when required) into momentum and thrust of exhaust gases expanding into a properly shaped nozzle.

Developing efficient and safe on-board chemical propulsion technologies and maximizing thrust production through optimal design of rocket components are becoming crucial objectives for aerospace applications, as witnessed by the number of papers in the field (see Hussaini and Korte 1996; Schley et al. 1997; Choudhuri et al. 2000; London et al. 2001; Reed 2004, among others). At present, no simple solution is available for design optimization: micro-rockets are complex systems, made of many simpler modules assembled together and interacting to produce the final performance (Rouse 2003). The main modules of a micro-rocket include storage systems for fuel and oxidizer, injection systems, combustion chamber, thrust generating nozzle, cooling system and micro-turbines. These different modules are interconnected by the mass and energy fluxes associated with the fluid moving inside the micro-rocket: once feeded into the combustion chamber, fuel and oxidizer react and heat up the mixture of exhaust gases which moves along the nozzle transferring heat to the walls, expanding and generating thrust.

Even though the configuration of micro-rockets is similar to that of large scale rockets, the smaller size makes their effective design more complex (Choudhuri et al. 2000; Rossi et al. 2002). Traditional design criteria, which were adequate for the large scale rockets must be revisited to fulfill the more stringent requirements associated with size reduction (Bayt and Breuer 2001). A typical effect of

miniaturization is the reduced residence time in the combustion chamber, which is usually counterbalanced by the use of higher energy-density fuels, characterized by a more explosive behavior and a larger heat release (Reed 2004). This implies (1) the use of high efficiency injection systems, able to obtain effective mixing in very small time, (2) the use of materials characterized by high mechanical and thermal resistance, and (3) the design of small scale cooling systems able to remove efficiently the heat produced by combustion. Furthermore, intensive use of energy and energy savings must be considered to improve micro-rocket performances over service life time.

State-of-the-art micro-rocket design solutions include the use of swirl injection systems to feed the combustion chamber, and regenerative heat exchange between combustion chamber and cooling system to recover energy from hot flue gases. The complex geometries of these micro-rocket components and the high degree of coupling between streams augment the number of possible alternative design configurations, increasing in parallel the risk of failure when developing innovative solutions. While on the one hand there are no general criteria to identify a priori the best performing design solutions, on the other hand the experimental testing of all trial configurations for micro-rocket components would require very long times and high prototyping costs. Therefore, objective approaches able to focus the experimental analysis on a reduced set of configurations are mandatory.

In this context, numerical analysis is becoming an emerging tool for the "virtual" testing of components *before* prototyping. A large number of design solutions can be evaluated in a short time and with reduced extra costs using self-validated numerical tools. Incorporating the relevant physics in the numerical model and setting up the model following the best practice guidelines suggested in the open literature ensure that the behavior of the system can be correctly simulated, at least qualitatively, and performances of design alternatives can be ranked objectively to identify the best promising. The experimental tests can then be focused on the verification of a subset only of "near-optimum" solutions. Then, the experimental data available at this stage can be used for the fine tuning of the virtual model, fitting calculated values with measured data.

In the numerical testing of micro-rocket components, combustion of non-conventional fuels, heat transfer in micro-channels and subsonic to supersonic flow transition are some of the complex phenomena which should be simulated properly for predictive testing. Additional modeling problems may arise due to micro-scale issues, since state-of-the-art numerical methodologies rely on the continuum assumption which may be not always satisfied in micro-devices. Furthermore, to replicate the real system complexity and the degree of interconnection of fluid

streams, coupling among combustion modeling, heat transfer and flow transition should be considered. This can lead to very complex and time consuming numerical simulations. In order to speed up the numerical analysis and to take a *real* advantage from numerical experiments over laboratory experiments, it is necessary to identify a proper decomposition strategy for the original problem (i.e. numerical qualification of micro-rocket performances and design optimization) such that (1) sub-tasks can be solved sequentially at a lower cost and (2) information obtained at each stage of the analysis can be gradually improved to obtain reliable information on the real system behavior. The problem decomposition stage is the core of the strategy: once all the relevant physical phenomena have been listed, the coupling between these mechanisms should be evaluated and hierarchically ranked to identify those sub-problems in which one physical mechanism may be considered prevailing, de-coupling that sub-problem from the others. This is the necessary condition for the problem decomposition approach to be effective for the analysis of complex systems.

In this paper, we describe the strategy adopted to aid the design of a micro-propulsion system which will be used for attitude control in micro-satellites of the Proba family (ESA) (Miotti et al. 2004). This included two steps: (1) decomposition of the problem and numerical analysis of sub-tasks, including tuning and self-validation of computational methodologies to fit each modeling challenge (combustion, subsonic/supersonic flow transition and heat transfer across solid boundaries) and "step by step" numerical testing of performances; and (2) evaluation of performances of the sub-optimal system as a whole and comparison with available experimental data. This approach has been successfully used for other applications (see for instance Cuda et al. 1999) and is expected to produce a benefit also in this context.

2 Configuration under study

A schematic of the thrust-generating part of the micro-rocket under study is provided in Fig. 1a. Figure 1b shows a three-dimensional view of the system and dimensions are summarized in Table 1.

The core of the micro-rocket is made of the combustion chamber, the nozzle and the cooling system. A central duct and a coaxial annular screw inject the fuel (ethanol) and the oxidizer (a mixture of oxygen and water vapor) in the combustion chamber. The swirling motion of the oxidizer is used to promote mixing with the inner stream of fuel. Mixing controls the chemical reaction process, determining composition, temperature and pressure of hot gases which are accelerated through the convergent–divergent part of

Fig. 1 a Sketch of the nozzle, indicating relevant dimensions and streams entering and leaving the apparatus. **b** 3-D model of the whole computational domain: combustion chamber and nozzle (*inner region, in light gray*), solid material (*dark gray*), and cooling fluid (*outer region, light gray*); **c** 3-D Mesh used to solve for the flow in the combustion chamber and nozzle
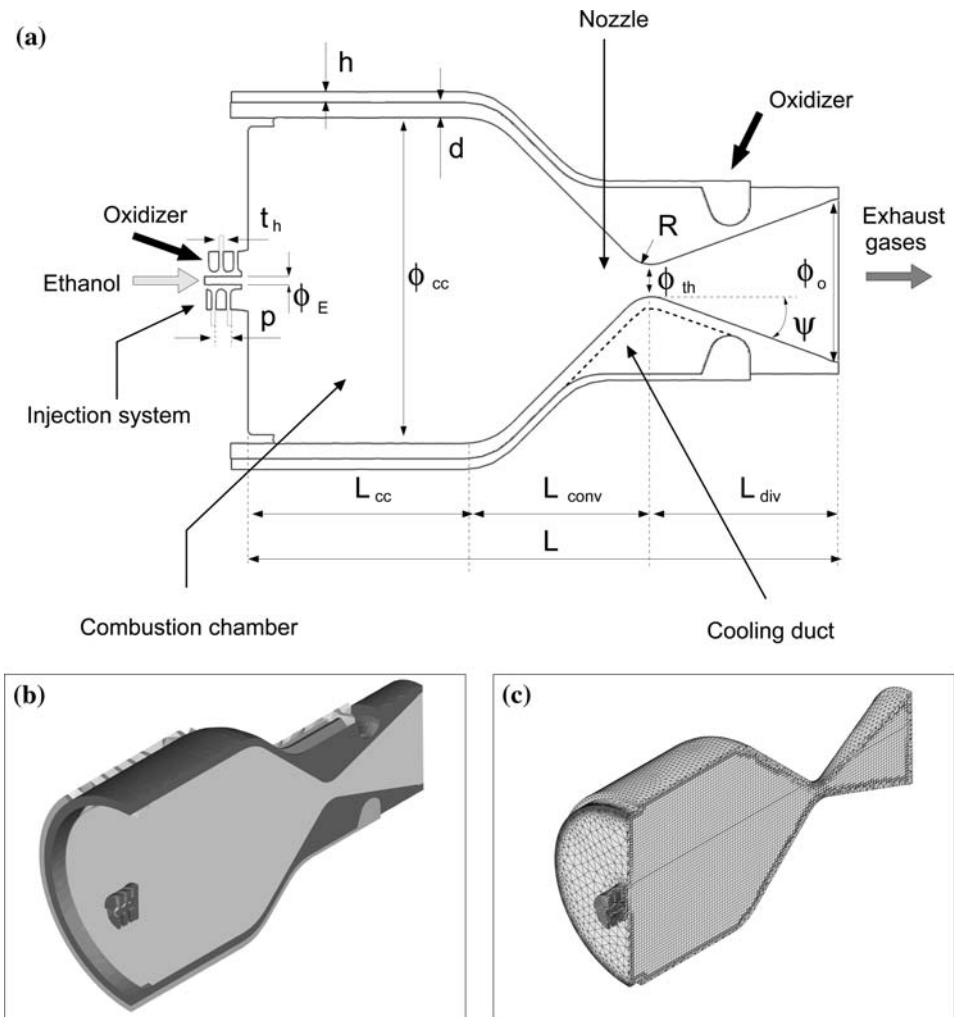
Table 1 Dimensions of micro-rocket

Overall length	L (mm)	30.3
Length of combustion chamber	L_{cc} (mm)	13.2
Length of convergent	L_{conv} (mm)	8.6
Length of divergent	L_{div} (mm)	8.5
Pitch of injection screw	p (mm)	2
Thickness of screw tooth	t_h (mm)	0.2
Diameter of injection duct	ϕ_E (mm)	0.2
Diameter of combustion chamber	ϕ_{cc} (mm)	15
Diameter of nozzle at throat	ϕ_{th} (mm)	1.5
Diameter of nozzle at exit	ϕ_o (mm)	7.5
Curvature radius at throat	R (mm)	1.5
Divergence angle	ψ (–)	20°
Wall thickness	d (mm)	0.7
Cooling vane thickness	h (mm)	0.5

the nozzle to produce thrust. Heat is transferred from the hot gases to the walls of the combustion chamber and nozzle. Here, heat should be efficiently removed to avoid excessive over heating and local temperature increase of the solid material, which can downgrade its mechanical resistance. In the configuration shown in Fig. 1, heat released by combustion is used to pre heat the oxidizer which moves inside the cooling system countercurrently to the exhaust gases expanding in the nozzle.

As shown in Table 1, the dimension of the micro-rocket range from few millimeters (cooling vane thickness, injection system diameter) to tens of millimeters (length of nozzle, dimension of combustion chamber). The spatial length scale is sufficiently large (1.5 mm at the throat) to simulate the flow as a continuum (Choudhuri et al. 2000). Yet, the values of the Knudsen number, i.e. the ratio between the molecular free path length and the representative physical length scale (the throat diameter), calculated a posteriori are in the range $0.01 < Kn < 0.1$. Since the flow is in the slip regime (Gad-el-Hak 1999), slip conditions have been implemented in the code to correctly simulate the behavior of micro-rocket modules (injection system, combustion chamber, nozzle and cooling duct).

3 Problem decomposition

Optimization of micro-rocket design implies that the assembly of injection system, combustion chamber, expansion nozzle and cooling system should guarantee that (1) fuel and oxidizer mix and burn completely; (2) most of the pressure energy contained in the exhaust gases is recovered along the nozzle to be converted in momentum; (3) the heat produced by the chemical reaction and convected by the expanding gases is efficiently removed by the cooling system preventing mechanical damages due to materials over-heating.

Mixing of reactants, chemical reaction, expansion in the nozzle and heat exchange across the solid shells are coupled to control micro-rocket performances. Yet, a problem decomposition can be identified to simplify the analysis. The sub-tasks identified for the micro-rocket design analysis are the following: (1) optimization of the nozzle shape, (2) analysis of mixing efficiency and chemical reaction in the combustion chamber, (3) heat production and heat transfer across the solid shells. The problem of shape optimization can be partially decoupled from the precise analysis of combustion, heat production and heat transfer. In fact, nozzle performances depend on nozzle shape and thermodynamical properties (pressure and temperature) of expanding gases, whichever the system used to produce the gases. Therefore, provided that the thermodynamical properties of the gases are properly estimated, nozzle shape optimization can be reduced to a 2-D, axis-symmetric problem in which the thrust generated by alternative geometrical configurations of the nozzle is evaluated, with significant savings in time and computational resources. Once a satisfactory configuration is found for the shape of the nozzle, the attention can be focused on the combustion chamber where the chemical reaction is supposed to generate the mixture of gases expanding in the nozzle. At this stage, the analysis should account for (1) the turbulent mixing of fuel and oxidizer generated by the injection system, (2) the combustion process and the heat produced thereof, and (3) the feedback effect that the shape of the flow-through combustion chamber (exhausting gases through the nozzle) may have on the internal flow, on mixing of species and on combustion. Physical arguments suggest that, since the flow becomes sonic at the throat, the analysis can be focused on the combustion chamber and the convergent part of the nozzle only. At this stage, if we are not concerned with the detailed chemistry of the process, the main effect of heat produced by the chemical reaction is the variation of density and velocity of gases moving in the combustion chamber. Therefore, heat transfer to the solid boundary can be neglected, being included only when the focus will be to evaluate the cooling system performances. Once a satisfactory configuration is found for the

combustion chamber, alternative configurations of the cooling system can be evaluated, eventually neglecting combustion dynamics and flow transition on the exhaust gas side, provided that the heat flux from the combustion chamber and along the nozzle wall can be properly estimated. The implementation of this problem decomposition strategy is discussed in the following: state-of-the-art numerical techniques and guidelines for model development are discussed first; results obtained from the analysis are then presented and compared with experimental data whenever available.

4 Numerical methods

The numerical simulations of nozzle, combustion chamber and cooling duct are performed using a commercial solver of the Navier–Stokes equations (StarCD®) based on a finite volume formulation. The code solves for the conservation equations of mass, momentum and enthalpy, calculating the flow, pressure, temperature fields and mass concentration of species (see the Appendix for details). Figure 1c shows a portion of the computational domain, divided into small computational volumes. Computational volumes are smaller near the walls and in the regions where large variations for the variables are expected, to allow the precise calculation of field gradients.

Figure 2 shows the links among conservation equations and the road map for their solution for a problem involving fluid flow, chemical reaction and heat transfer. Equations are written in discretized form for each finite volume of the computational domain. Cartesian velocities, pressure, temperature and concentration of species are evaluated at cell centers, and contravariant volume fluxes are evaluated
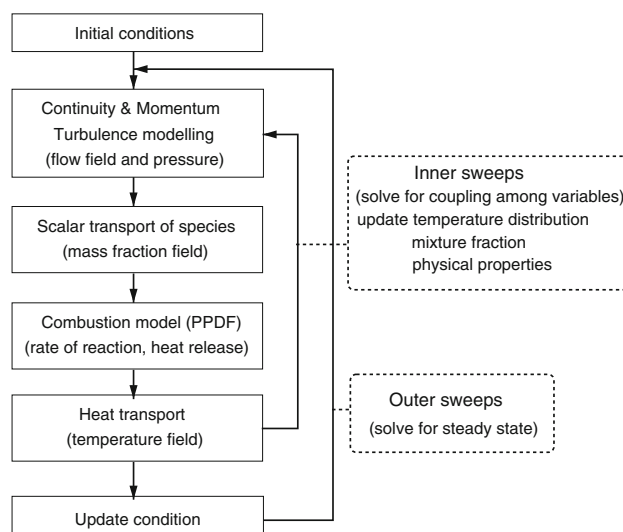
Fig. 2 Road map for the solution of linked conservation equations

at cell faces. Flux discretization is obtained by a third order (QUICK) scheme. As shown in Figure 2, coupling among mass, momentum and energy equations is considered by inner sweeps in the solution process and convergence toward a steady state is obtained through outer sweeps. Conservation of mass and momentum (Eqs. 6 and 7 in the Appendix) are solved using the SIMPLE algorithm (Patankar and Spalding 1972) which is based on operator splitting and predictor/corrector stages. Equations for each dependent variable are decoupled and linearized, and then solved using the conjugate gradient (CG) method. The pressure correction equation (Poisson equation) is solved using a multigrid algorithm.

According to the steps indicated in Fig. 2, the 3-D flow field is solved first and used to calculate (1) the transport/dispersion and reaction of chemical species (Eq. 13 in the Appendix) and (2) the heat released by the progress of the chemical reaction (see Issa et al. 1991 for details). The heat flux from chemical reaction is used to solve the chemico-thermal enthalpy balance (Eq. 18 in the Appendix) and to obtain the temperature field in the fluids (flue gases and cooling flow) and across the solid (Eq. 19 in the Appendix). At each inner iteration, updated values of temperature and mass fraction of species are used to modify fluid properties (ideal mixture of gases) and to iterate again on velocity and pressure. This procedure is repeated until stable values are found for all the variables. Then, an outer iteration starts toward the calculation of steady state conditions.

In this work, specific modeling issues originate from (1) the strong swirling motion generated by the injection system, (2) the chemical reactions and heat production, and (3) the subsonic to supersonic flow transition in the nozzle. These are described briefly in the following.

4.1 Turbulent swirling flow

The screw injection system is a crucial portion of the micro-rocket under study and accurate modeling of the turbulence generated by the swirling flow is necessary (1) to simulate mixing between fuel and oxidizer, (2) to evaluate the progress and efficiency of the combustion process, and (3) to calculate thermodynamical properties (pressure and temperature) of exhaust gases before expansion.

Coaxial swirling flows are increasingly used in many industrial configurations (i.e. cooling systems, fluid mixers, industrial burners and propulsion apparatuses) and usually consists of a main central jet and a coaxial swirling stream. The fluid dynamics of swirling flows has been extensively investigated for both non-reacting and reacting flows. Experiments performed on cold, coaxial, swirling jets (Huang and Tsai 2001) show that in these configurations

the entrainment of fluid by the central jet is dramatically modified by the interaction with the coaxial swirling flow. Specifically, a strong increase in the jet spreading angle is produced by the formation of a central stagnant zone and a recirculation bubble of fluid. Following Al-Abdeli and Masri (2003), the main parameters controlling the dynamics of these large scale structures are the swirl number, i.e. the ratio of the axial flux of the angular momentum to the axial flux of the axial momentum, and the streamwise velocity (see Park et al. 1998 among others). These structures are often exploited to enhance the mixing of species, with significant benefit for applications involving combustion processes.

One of the main difficulties associated with the numerical simulation of swirling flows is turbulence modeling. Many numerical simulations (see for instance Battaglia et al. 2000, Jakirlic et al. 2004 and Snegirev et al. 2004) have shown that simple turbulence models (as eddy viscosity, $k-\varepsilon$ models) fail to capture the anisotropy typical of strain and Reynolds stresses produced in the flow by the action of centrifugal forces. In these cases, modified first-order or second-order closure relations are required to reproduce the effect of flow curvature on turbulence (Sankaran and Menon 2002). Previous works on the simulation of swirling flames (Snegirev et al. 2004; Eiamsa-ard et Promvonge 2007) have shown that good results can be obtained using Algebraic Stress Models and Reynolds Stress Models. Other works on swirling flows have shown that good results can be obtained using simpler, modified versions of the $k-\varepsilon$ model. In this work, we chose to use a RNG $k-\varepsilon$ model (Yakhot and Orszag 1986) which represents a satisfactory and reasonable choice by which a precise balance between accuracy and time/costs of the simulation can be achieved: the effect of mean flow distortion on turbulence is incorporated by considering an additional term in the dissipation equation (Eq. 10 in the Appendix); compressibility and buoyancy effects can be considered as in the standard $k-\varepsilon$ model (see the Appendix for details).

4.2 Combustion model

The second critical point for the analysis of the micro-rocket is the simulation of the reacting flow. Reaction rates depend on two main mechanisms: (1) the transport of species, determining the local concentration of reactants and (2) the chemical kinetics. Transport and mixing of species is controlled by the flow dynamics, with the large scale structures contributing to bulk transport and the small scale structures contributing to micro-mixing; therefore, both scales must be considered to get a realistic picture of the reacting environment. Chemical kinetics are inherently complex, with most of the chemical reaction schemes

involving hundreds of intermediate reacting species (Hsu and Mahalingam 2003; Bohn and Lepers 2001). A dimensionless parameter useful to quantify the relative importance of transport of reactants and chemical kinetics is the Damkohler number, Da, which represents the ratio between the characteristic time for the transport of species and the characteristic time for chemical reactions. A large Damkohler number, $Da \gg 1$ corresponds to a chemical reaction which is fast in comparison to all other processes. In this case, the rate controlling step is the turbulent mixing. A small Damkohler number, $Da \ll 1$ corresponds to a chemical reaction which is slow in comparison to all other processes. In this case, the rate controlling step is the chemical reaction. For unpremixed (or diffusion) turbulent reactions, as the one considered here, Da is $\gg 1$, i.e. the chemical reaction is controlled by the turbulent mixing.

In this work, the chemical reaction occurring in the combustion chamber is ethanol oxidation at high temperature, given by:

$$C_2H_5OH + 3O_2 \rightarrow 2CO_2 + 3H_2O. \tag{1}$$
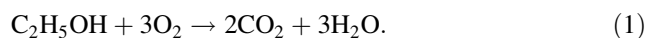
Oxygen is obtained from peroxide decomposition, and the reaction occurs in excess water vapor. A complex reaction scheme for ethanol combustion involving more than 56 species and 351 chemical reactions has been developed by Marinov (1999). Including such a detailed description of the ethanol oxidation in a three-dimensional numerical simulation would be extremely expensive, since the mass balance of 56 chemical species should be considered for each computational volume in the domain. Furthermore, such a detailed description is not required if we are not interested in simulating the formation of specific products generated by the chemical reaction. Our focus in this work is to simulate precisely the thermal field produced by ethanol combustion to account for variations in gas pressure, density and velocity which control the motion of gases toward the nozzle. Therefore, to contain the costs of the CFD simulation, we schematize the combustion process using a single step reaction mechanism. Since this simplified description gives an approximate picture of the real thermal balance, we use the tunable parameters of the combustion model to fit the main thermal characteristics of the oxidation process with available experimental data.

In mixing controlled reactions, turbulent transport modeling must be considered for realistic simulations. In this work, effects of turbulent mixing are accounted for using a presumed probability density function (PPDF) model which is particularly suited for fast reacting, unpremixed systems in which the time for convection and diffusion of reactants is much larger than the time for reaction, and the reaction process is controlled by turbulent mixing (Zhou et al. 1999). In PPDF models, a conserved scalar f, called the mixture fraction and defined as:

$$f = \frac{m_f}{m_f + m_o} \tag{2}$$

where, m_f is the mass of fuel and m_o is the mass of oxidizer, is used to describe the progress of the turbulent mixing process. The transport equations for the mixture fraction and its variance (Eqs. 14 and 15 in the Appendix) are used to determine the values of the local mass fractions of chemical species. The instantaneous mass fraction of fuel, oxidizer and products is calculated from (1) the mean local value of f, solved for by the transport equation, (2) the local value of the variance of f, which accounts for fluctuation produced by turbulence, and (3) from the "presumed" probability density function (Eq. 16 in the Appendix) for f (see Richardson et al. 1953, for details). The heat released by the progress of the chemical reaction is then calculated from the enthalpy balance.

4.3 Transitional flow

The numerical simulation of flow in the nozzle is complex because the flow is transitional, i.e. subsonic in the convergent, sonic at the throat and supersonic in the divergent, where shock waves produce discontinuities in the field variables. Therefore, the first issue was to identify and validate a suitable numerical methodology to simulate transitional flows.

Transitional flows are usually described using 1-D theory based on momentum and enthalpy conservation equations, neglecting the viscous forces acting at walls. We performed preliminary numerical simulations (1) to identify the most appropriate boundary conditions to be used for the simulation and (2) to compare Navier–Stokes calculations with the reference solution available from 1-D design theory. To set up the numerical simulation, we considered a standard design nozzle, characterized by convergent angle $\psi_{conv} = 22.5°$, divergent angle $\psi_{div} = 4°$, throat diameter $\phi_{th} = 30$ mm, delivering a critical flow rate of air ($T = 1,500$ K in the throat). The specific mass flux delivered by this nozzle is the same expected for the micro-rocket. Yet, nozzle dimensions are 20 times larger than the nozzle of the micro-rocket under study, and no slip conditions can be used at nozzle wall for these numerical tests. We performed axis-symmetric simulations for a slice of the nozzle (1/36), assuming conservation of stagnation enthalpy through the nozzle and imposing stagnation pressure and temperature at inlet ($p_{cc} = 742.5$ kPa, $T_{cc} = 1,800$ K) and a value of pressure at outlet ($p_o \leq 10^5$ Pa) as boundary conditions. We solved for the flow under different flow regimes (sub-sonic, sonic and supersonic) changing the value of pressure at the outlet from the stagnation value down to the desired outlet value. We found that a transient simulation using a fixed value of

pressure at inlet (stagnation) and a value of pressure at outlet gradually decreasing to the target value allows to obtain a converged solution which ever the flow conditions in the nozzle. We compared pressure profiles along the nozzle axis calculated in this way against those expected from 1-D theory (results not shown). We found a satisfactory agreement between numerical and analytical pressure profiles along the nozzle coordinate, and small deviations due to viscous effects: specifically, solution of Navier–Stokes equations showed that (1) the outlet pressure should be reduced more than the calculated 1-D theoretical value to have sonic flow at the throat, that (2) sharp curvature radius at throat may promote the formation of a "vena contracta", and that (3) pressure drops due to viscous losses (which are neglected in 1-D theoretical model) are almost negligible in the supersonic regime. We found that the minimal domain resolution to obtain grid-independent results was also adequate to capture correctly normal shocks in the divergent.

Then, we considered the simulation of a down-scaled nozzle (throat diameter equal to 1.5 mm). Due to the size reduction the flow inside the nozzle is now in the slip regime, for which slip boundary conditions need to be implemented at nozzle walls. Slip boundary conditions were implemented in the finite volume solver in the form reported by Gad-el-Hak (1999) using user defined subroutines (see Eqs. 11 and 12 in the Appendix).

5 Results

5.1 Thrust generation system

As indicated by the problem decomposition analysis, the first step to focus on was the identification of the "optimum" shape of the nozzle to recover the pressure energy from hot flue gases and to produce the thrust required for point positioning. A thrust level of about 1 N was considered sufficient for keeping spacecraft attitude control during firing operations and for reducing the energy losses during trajectory manoeuvres (impulsive manoeuvres) (see Miotti et al. 2004).

We used the methodology described in Sect. 4.3 to perform simulations for a number of trial design configurations of the micro-rocket nozzle (see Table 2) with the final object of identifying guidelines for nozzle shape optimization to maximize the thrust. Geometrical design constraints were formulated as follows: inlet diameter and throat diameter should be considered fixed (ϕ_{cc} = 15 mm, ϕ_{th} = 1.5 mm) and overall nozzle length should not exceed 20 mm. The first trial configuration was characterized by convergent angle, ψ_{conv} = 60°; divergent angle ψ_{div} = 20°; outlet diameter equal to ϕ_o = 6.20 mm; total length of the nozzle L = 10.3 mm; curvature radius R = 0.2 mm. The large divergent angle (about twice the value of standard design nozzles) is typical of nozzles operating at open space pressure ($p_o \simeq 0$ Pa).

For all the configuration tested, we assumed homogeneous inflow of an (ideal) mixture of gases from the combustion chamber (mass flow rate equal to 0.37 g/s, equivalent molecular weight $M \simeq 21$ kg/kmol, specific heat ratio γ = 1.2, stagnation pressure 3×10^5 Pa and stagnation temperature 2,200 K) and we evaluated nozzle behavior for two reference working conditions, corresponding to atmospheric pressure ($p_o = 10^5$ Pa) and open space pressure at outlet. The flow is supersonic in both conditions, with a shock wave inside the divergent for external pressure at atmospheric, and a free expansion outside the divergent for external pressure at vacuum. In the last case, to avoid the simulation of the expansion in the outer plenum, we fixed the value of pressure at the nozzle outlet equal to the adaptation value calculated solving 1-D isentropic equations for the given geometry (p_o = 1,926 Pa for simulation A).

Table 2 Geometrical parameters for alternative nozzle configurations and calculated performances: flow rate, thrust, momentum flux, pressure contribution

SIM	ψ_{conv} (°)	ψ_{div} (°)	L_{div} (mm)	L_{noz} (mm)	p_{ada} (Pa)	$\dot{m}$ (g/s)	S (N)	$\int d\dot{m} \cdot v$ (N)	$\int \Delta p \, dA$ (N)
A	60	20	6.7	10.59	1,926.05	0.334	0.799	0.725	7.44×10^{-2}
B	60	10	6.7	10.59	6,672.98	0.322	0.749	0.655	9.32×10^{-2}
C	60	10	13.3	17.19	1,926.05	0.318	0.621	0.498	12.29×10^{-2}
D	60	10	3.7	7.59	16,080.5	0.348	0.729	0.616	11.24×10^{-2}
E	60	5	6.7	10.59	18,486.5	0.342	0.709	0.587	11.21×10^{-2}
F	45	10	5	11.75	10,543.6	0.36	0.787	0.681	10.59×10^{-2}
G1 (R = 0.2 mm)	45	20	8.5	15.25	1,185	0.365	0.9713	0.871	1.003×10^{-1}
G2 (R = 1.5 mm)	45	20	8.5	15.78	1,185	0.368	0.9699	0.874	9.498×10^{-2}
G2$_{atm}$	45	20	8.5	15.78	10^5	0.349	0.226	0.222	4.16×10^{-3}

Last three rows effect of the radius of curvature at throat

For the first trial configuration, we checked the grid independence of calculated quantities comparing the results obtained using two different grid resolutions (a fine geometry made of 4,500 finite volumes and a very fine geometry made of 6,000 finite volumes); we found differences less then 3% in the pressure profiles calculated along the nozzle axis, indicating that the fine mesh was sufficiently resolved for the analysis. We used a similar resolution for all the other configuration tested.

To compare the performances of different nozzle configurations we calculated isentropic efficiency, η, and thrust, S, at the outlet section, as follows:

$$\eta = \frac{\overline{c_{cc}}^2 - \overline{c_o}^2}{\overline{c_{cc}}^2 - \overline{c_{os}}^2}, \tag{3}$$

and

$$S = \int_{A_o} d\dot{m} c_o + \int_{A_o} (p_o - p_{ext}) dA, \tag{4}$$

where $\overline{c_{cc}}$ is the average velocity at inlet, $\overline{c_o}$ is the average calculated velocity (2-D simulation) at outlet, $\overline{c_{os}}$ is the average velocity (isentropic) at outlet, $d\dot{m} c$ is the differential momentum flux, A_o is the outlet section area, p_o is pressure at outlet section, p_{ext} is outer environmental pressure ($p_{ext} \simeq 0$). Values calculated for thrust are shown in Table 2. For the first trial configuration (label A in Table 2) we found isentropic efficiencies equal to $\eta = 0.011$ and 66.11% for the nozzle working at atmospheric and open space pressure, respectively. The thrust generated in these condition was $S = 0.256$ and 0.799 N, respectively. As expected, the large divergent angle improves nozzle performances when the external pressure is well below the atmospheric value.

Table 2 summarizes results obtained for all the different configurations investigated when gases expand to open space pressure. The first four columns identify the geometry of the nozzle, subsequent columns show the value of pressure imposed at the outlet section, the mass flow rate delivered by the nozzle and the thrust produced, which is due to gas momentum and gas overpressure at the nozzle exit. The mass flow rate delivered by each nozzle under the same stagnation conditions is different because viscous effects may play a major or minor role depending on the configuration. As observed by Ketsdever et al. (2005), viscous losses may become large enough to downgrade performances in micro-scale nozzles. Results can be summarized as follows: (1) for fixed convergent/divergent angles (see configurations B, C, D), the thrust has a maximum for intermediate values of the divergent length (i.e. configuration B); (2) for fixed divergent length and convergent angle (see A, B, E) the thrust increases with the divergent angle, and thus with the area of the outer section;

(3) for a fixed divergent angle (see D, F) the thrust can be increased by reducing the convergent angle. These trends are consistent with results reported by Ketsdever et al. (2005). At this stage of the work, we did not considered necessary to established a direct comparison with experimental data: our object was to identify a best promising geometry rather than predicting precisely the value of thrust produced by the nozzle. Experimental data become necessary to validate the model when quantitative predictions are required. We found an optimal balance between design constraints and nozzle performances for configuration G, characterized by convergent angle, $\psi_{conv} = 45°$; divergent angle $\psi_{div} = 20°$; outlet diameter equal to $\phi_o = 7.50$ mm; total length of the nozzle $L = 15.25$ mm. For this last configuration, we calculated variation in performances due to an increase in the radius of curvature at the throat. Larger radii are expected to smooth the flow path from the convergent to the divergent, reducing losses. Specifically, we considered a change in the curvature radius from $R = 0.2$ mm (corresponding to all the configuration already examined) to $R = 1.5$ mm. L_{conv} and L_{div} were increased slightly to leave the inlet and outlet section areas unchanged. Results of this comparison are summarized in the last rows of Table 2. For open space pressure, the thrust generated by configuration G2 is near to the target value of 1 N for which the nozzle was originally designed to operate. The effect of curvature radius in this condition is found to be almost negligible.

Figure 3 shows results obtained from the numerical simulations of configuration G2. Mach number isocontours in a section through the axis of the nozzle and pressure profile along the nozzle coordinate are shown for the gas expanding to atmospheric pressure (Fig. 3a, c) and to open space pressure (Fig. 3b, d). When the pressure at the outlet section is 10^5 Pa, Mach number isocontours (Fig. 3a) show a shock wave in the divergent and under-expanded flow in the near wall region. The pressure variation along the nozzle axis (Fig. 3c) increases steeply at shock location. Figure 3b shows the results calculated when the pressure at nozzle outlet section is $p_o = p_{ada} = 1,185$ Pa. Mach number isocontours indicate that the flow is supersonic everywhere in the divergent. The pressure profile along the nozzle axis (Fig. 3d) decreases gradually, in agreement with the trend predicted by 1-D theory. The last configuration was chosen as the final nozzle design for all subsequent steps of the work.

5.2 Injection system and combustion efficiency

The following step of the analysis was to evaluate the mixing produced by the injection system which determines the combustion efficiency and the thermodynamic properties of hot gases expanding into the nozzle. The computational

Fig. 3 Mach number isocontours (*top*) and pressure profile along the nozzle (*bottom*) for external pressure at atmospheric (**a**, **c**) and at vacuum (**b**, **d**)
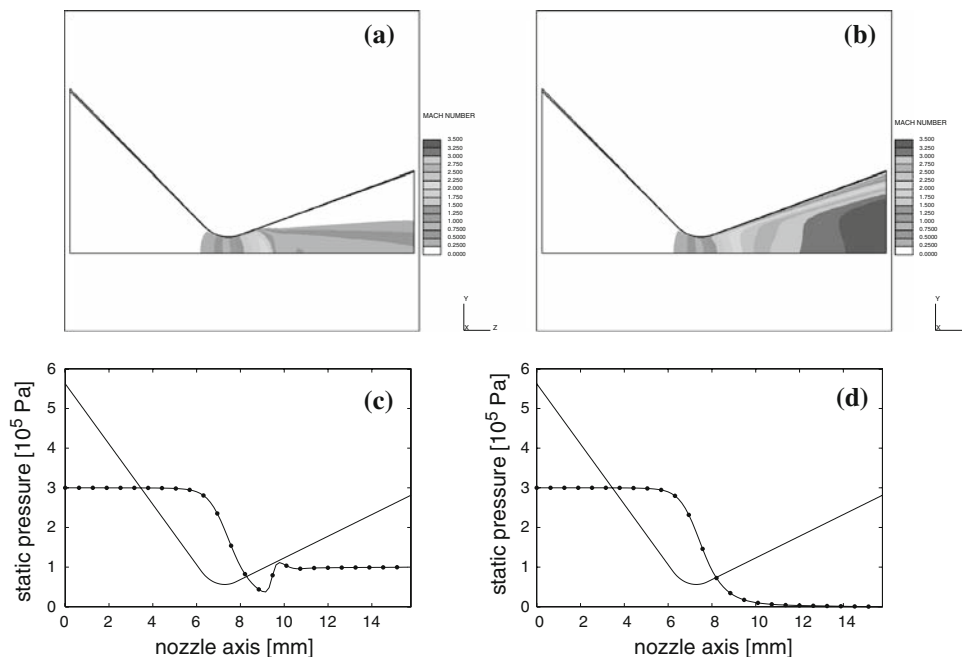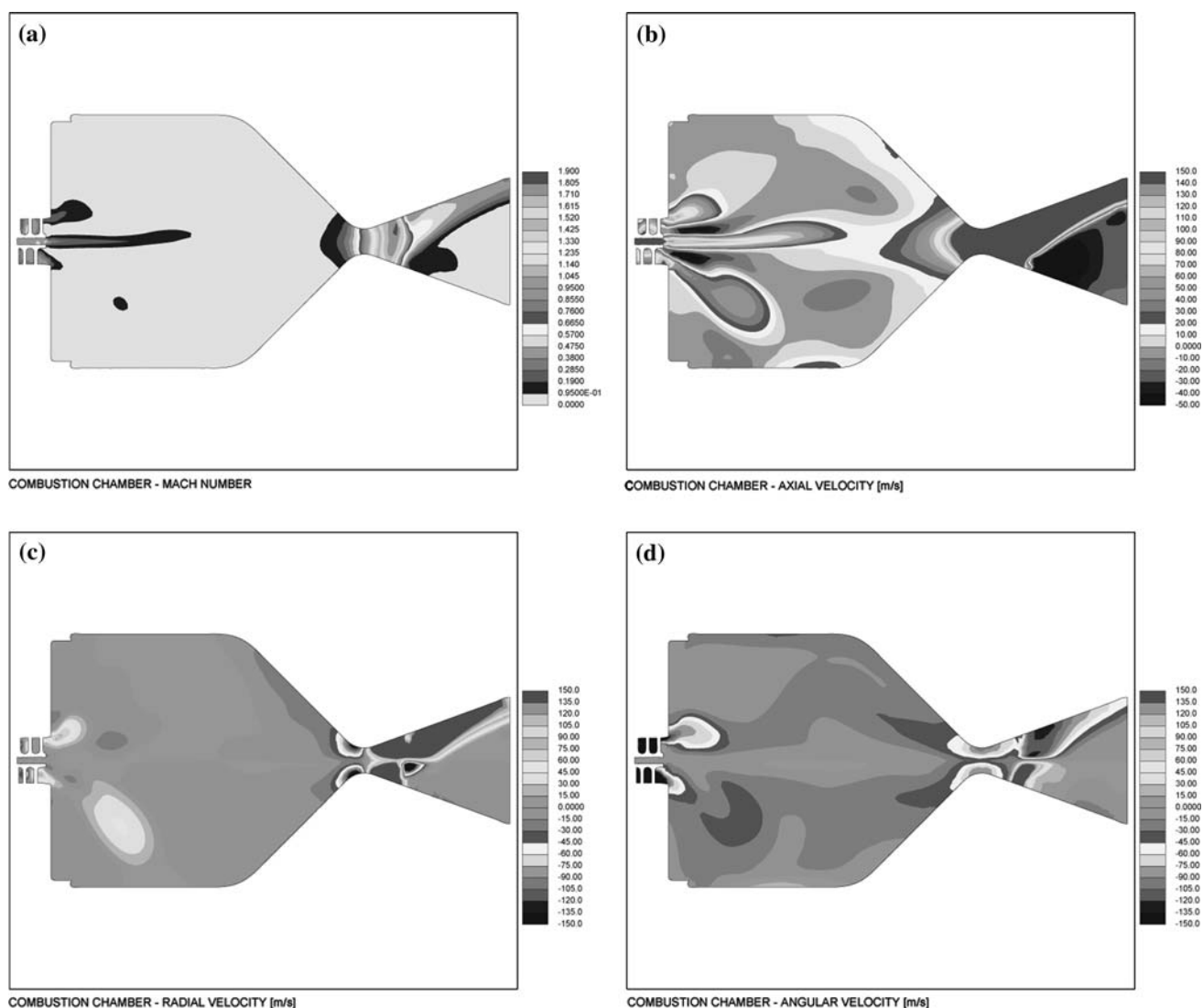
domain considered is shown in Fig. 1c and includes the injection system, the combustion chamber and the nozzle. At this stage, these modules can be considered decoupled from the outer coaxial cooling system assuming adiabatic walls for the combustion chamber and nozzle. Preliminary simulations demonstrated that at least the convergent portion of nozzle should be included in the computational domain to simulate precisely the flow in the combustion chamber, since the throat of the nozzle is the first section which can be defined, in a simple way, as the outlet boundary of the combustion chamber.

At this stage of the work, we focused on the behavior of the injection system for the nozzle expanding the gases at atmospheric pressure. Boundary conditions for the simulation are (1) fixed mass flow rate of ethanol and oxidizer at the screw inlet and (2) pressure imposed ($p_o = 100$ kPa) at the outlet section of the nozzle. A reference pressure value is also given for the combustion process ($p_{cc} = 300$ kPa). The conditions given above correspond to a strong swirling flow generated by the injection system, and critical flow for the mixture of reactants and exhaust gases at the throat of the nozzle. Since the flow becomes sonic at the nozzle throat, the specific value of pressure imposed at nozzle outlet is expected to have no significant feed-back on flow and combustion dynamics inside the combustion chamber. Therefore, no modifications of the flow inside the combustion chamber are expected when the outlet pressure will be lowered to open space values.

Figure 4a shows the isocontours of the Mach number in the combustion chamber and in the nozzle. The shock wave developing at the throat is evident from the contours. The maximum value of Mach number (1.8) is found about 2

diameter downstream the throat. This value is in agreement with the result of the 2-D, axis-symmetric calculation shown in Fig. 3a ($Ma = 2.0$). Also the position of the shock is similar. The same considerations hold for the pressure along the nozzle axis, with similar minimum value for the pressure at the point where the shock develops. Differently from the axis-symmetric simulation, the flow in the divergent is not symmetric, with the expanding flow attached to the nozzle wall in a time dependent way. This effect is due to an instability of the numerical solution arising in the azimuthal direction, most likely triggered by the rotational flow in the combustion chamber, and by the outlet pressure boundary. Since the shock is inside the nozzle, instabilities do not prevent the fluid coming from the outlet section to flow back into the divergent part of the nozzle.

Velocity values in the combustion chamber (see Fig. 4b–d) range from 50 to 150 m/s at the point of injection of oxidizer and fuel, to 20 m/s in the bulk of the chamber, rising up to 500 m/s in the converging part of the nozzle and to 1,800 m/s downstream the throat, in the diverging region. To describe the flow in the combustion chamber, the axial, radial and azimuthal components of velocity shown in Fig. 4b–d are represented using isocontours whose upper value is fixed in the subsonic range. We observe that the angular motion produced at the screw exit propagates into the combustion chamber. The intensity is between 0 and −26 m/s in the bulk of the chamber. The interaction between the axial jet of ethanol and the swirling flow of oxidizer generates a strong recirculating motion (negative axial velocities) in the chamber, with velocity values up to −50 m/s right downstream the ethanol

COMBUSTION CHAMBER - MACH NUMBER

COMBUSTION CHAMBER - AXIAL VELOCITY [m/s]

COMBUSTION CHAMBER - RADIAL VELOCITY [m/s]

COMBUSTION CHAMBER - ANGULAR VELOCITY [m/s]

Fig. 4 Components of velocity calculated in combustion chamber and nozzle: **a** isocontours of Mach number in axial section of micro-rocket: a shock wave forms downstream the throat of the nozzle; **b** axial component; **c** radial component; **d** azimuthal component. Scales are upper bounded to cut supersonic values

injection point. As suggested by Huang and Tsai (2001), this strong recirculation is crucial to promote enhanced mixing between fuel and oxidizer increasing the combustion efficiency.

We calculated also the thrust produced by the exhaust gases at the nozzle outlet. For outlet boundary conditions corresponding to atmospheric pressure, we found a value of 0.194 N for the thrust, which is in agreement with the value ($S = 0.226$ N) calculated from 2-D axis-symmetric simulation (see configuration $G2_{atm}$ in Table 2). This value is in the range measured in the lab at atmospheric conditions 50–550×10^{-3} N for a prototype of the micro-rocket, as reported by Scharlemann et al. (2006).

The flow field in the combustion chamber determines the transport and dispersion of reactants, their rate of reaction and the formation of products. Figure 5a shows the isocontours of the fuel to mixture ratio normalized to the stoichiometric ratio; Fig. 5b shows the temperature calculated in a section of the combustion chamber through the axis. The fraction of fuel, which is more than 5.5 the stoichiometric value at the injection point, decreases as the fuel mixes in the combustion chamber. Stoichiometric conditions (unit isocontour) are reached as the fuel is transported and dispersed in the central portion of the combustion chamber. This region corresponds to a significant part of the volume indicating that, due to the swirling action, ethanol is efficiently mixed with oxygen. A small amount of ethanol (maximum local mass fraction 0.35) is still present at the throat of the nozzle where the mass fraction of unreacted oxygen is about 0.18. We calculated
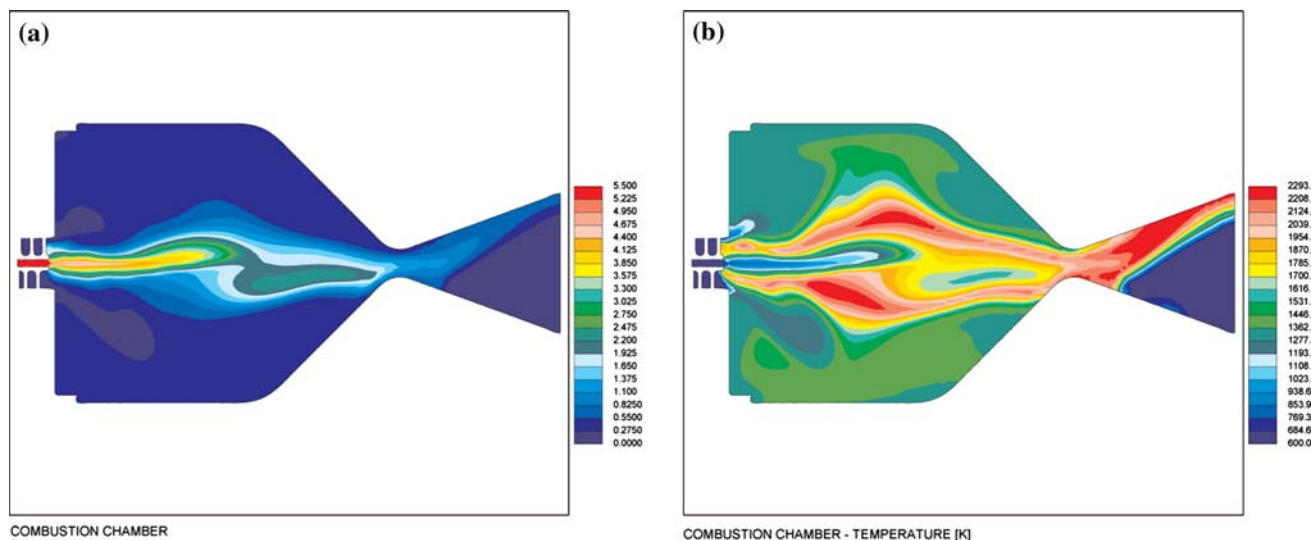
Fig. 5 **a** Isocontours of fuel to mixture ratio scaled to stoichiometric ratio; **b** isocontours of temperature

the efficiency of the combustion chamber considering the fraction of fuel burnt at the throat of the nozzle, which can be considered as the exit of the combustion chamber and we found that 90% of ethanol is burnt at this section. This value of combustion efficiency is in line with values expected for micro-rockets (see Reed 2004), indicating that the original design of the screw injection system performs satisfactorily and no further optimization of the injection system is required at this stage.

Figure 5b shows temperature isocontours. Temperature isocontours follow the dispersion of fuel and oxidizer, with the combustion in the near stoichiometric region producing the largest heat release and temperature increase in the fluid. In this simulation, the wall of the combustion chamber and nozzle are considered adiabatic. Therefore, gas heating due to the chemical reaction is over estimated because no heat dissipation is possible through the nozzle wall. The temperature of fuel and oxidizer is 600 K at the screw inlet. The temperature increases in the region where the reaction proceeds, heating the fluid in the chamber. The average value of temperature in the combustion chamber is about 1,400 K, with maxima about 2,300 K in the combustion region.

5.3 Assembled system: efficiency of cooling system, mechanical resistance and thrust

The objects of the last step of the work were (1) to evaluate the thrust generated by the expansion of exhaust gases in open space, (2) to evaluate temperature distribution in the solid shell enclosing the combustion chamber and nozzle, and (3) to evaluate effectiveness of the cooling system which should also be used for pre-heating of reactants. The cooling system is made of an annular channel surrounding the combustion chamber and the rocket wall. A section of the cooling channel made along the axis of the micro-rocket is shown in Fig. 7. The through-flow section changes with position and is designed to guarantee a sufficiently large velocity of the cooling fluid to promote convective heat removal from the inner wall. Sixteen fins protruding from the inner wall into the cooling channel are considered in the first trial design to promote the heat transfer in the nozzle region, where the surface exchanging heat is minimum and the heat flux is maximum.

At this stage, the computational domain, previously shown in Fig. 1b, includes the volume of the combustion chamber and nozzle (inner part in light gray) filled by the mixture of fuel, oxidizer and combustion products, the solid shell enclosing the combustion chamber and nozzle (dark gray), and the cooling vane (outer part in light gray) filled by cooling fluid. The overall domain is made of 580,000 cells. Table 3 summarizes the properties of the cooling fluid, which is the mixture of oxygen and water vapor used as oxidizer in the combustion chamber. The fluid is considered compressible, and physical properties are calculated as a function of temperature and pressure using CHEMKIN polynomials. Table 4 summarizes the thermal properties of the solid shell corresponding to the

Table 3 Properties of the cooling fluid

	Oxygen	Water vapor
Mass fraction	0.33	0.67
Molar fraction	0.21	0.79
Molecular weight	32	18
Mixture		
Molecular weight	20.76 kg/kmol	

Table 4 Properties of nimonic

Temperature (°C)	Specific heat (J/kg K)	Thermal conductivity (W/m K)
20	419	10.89
100	461	12.10
200	502	13.57
300	502	14.99
400	544	16.33
500	544	17.67
600	586	18.63
700	628	20.56
800	628	22.23
900	670	24.03
1000	670	26.21

Density 8,010 kg/m^3; *Melting range* 1,290–1,345°C

combustion chamber and nozzle which is made of nimonic, a nickel–chromium alloy with good mechanical properties and oxidation resistance at high temperatures.

We performed a fully-coupled simulation of flow in the combustion chamber and nozzle at steady state conditions considering the additional effect of heat transfer across the solid material and the flow of the cooling fluid on the external side of the solid shell. The same boundary conditions as described in Sect. 5.2 are used to simulate the flow of hot gases. Additional boundary conditions applied for the cooling fluid are fixed mass flow rate of the cooling fluid (0.32 g/s), inlet temperature ($T_{in} = 480$ K) and pressure value at the outlet section ($p_{out,cd} = 330$ kPa). The outer wall of the cooling duct is considered adiabatic. This is a conservative assumption, which allows to evaluate the cooling efficiency of the solid shell with reference to worst case conditions. We checked the numerical convergence

for the thermal problem considering the balance among the heat fluxes transferred from the exhaust gases to the solid shell, across the solid shell and from the solid shell to the cooling fluid. At steady state, the heat transferred was equal to 5.52 W.

Results calculated from the simulation of the whole system at open space pressure will be now discussed with reference to those obtained in the previous phases of the work. Figure 6 shows isocontours of the Mach number: simulating the heat transfer from exhaust gases to the shell, the maximum value increases to 2.8. This value is larger than in the axis-symmetric simulation or in the simulation of combustion chamber and nozzle without heat exchange due to the variation of the velocity of sound, which depends on the local temperature of the gas. The thrust calculated for the system is equal to 0.83 N and is again in good agreement with the value calculated by the 2-D axis-symmetric simulation (0.9699 N for configuration *G*2 in Table 2) and with the value reported for the apparatus after experimental tests in vacuum (see Scharlemann et al. 2006).

Figure 6b shows the temperature of the fluid in the combustion chamber, the temperature inside the solid material and the temperature of the cooling fluid. As expected, temperature isocontours in the combustion chamber are slightly lower than those already calculated when the heat transfer to the wall was neglected and the outlet pressure was equal to p_{atm} (see Fig. 5b). In fact, the heat transfer from hot gases to the cooling fluid (5.52 W) is significant given the small dimensions of the micro-rocket.

According to micro-rocket design requirements, excessive increase in temperature of the shell is to be avoided to reduce the risk of mechanical failure. In the micro-rocket under study, this is obtained (1) by exploiting the high
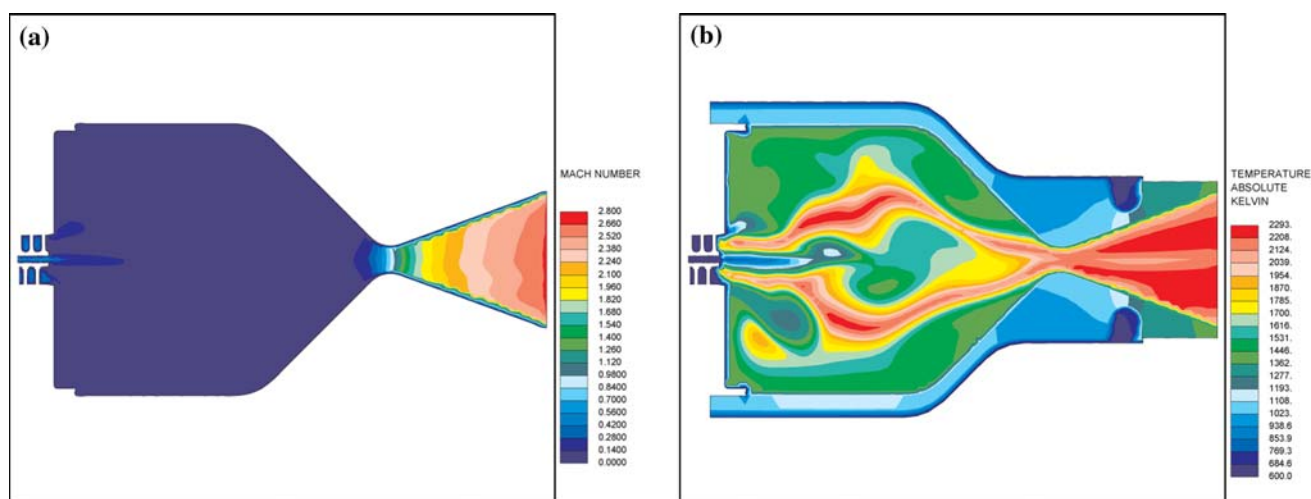
Fig. 6 a Isocontours of Mach number for the assembled system when outlet pressure is that of open space. Maximum Mach number is 2.8, in agreement with the result of axis-symmetric simulation; **b** temperature isocontours when hot gases exchange heat across the solid shell

velocities of the cooling fluid moving in the narrow co-annular channel around the shell and (2) by enhancing the heat transfer from the solid shell to the cooling flow using the finned surfaces in the most critical region. In the present configuration, the heat transferred across the wall of the nozzle is characterized by a highly non homogeneous distribution both in the streamwise and in the azimuthal directions. Figure 7 shows the variation of quantities related to heat transfer across the solid shell; the variation of the heat flux along the axial coordinate of the nozzle is shown in Fig. 7a for two different azimuthal positions: the solid line refers to a section of the cooling system aligned with one fin, the dashed line refers to a section of the cooling system placed midway between two fins. A peak is observed on both lines at the throat of the nozzle, where the heat exchange surface is at minimum on the inner side. The fins are used in this region to improve the heat transfer coefficient at the cooling side: the maximum pressure drop along the channel is fixed and this imposes an upper limit to the cooling fluid velocity and to the convective heat transfer coefficient. Figure 7b shows the variation along the axis of the cooling fluid velocity, averaged over the thickness of the channel. The same azimuthal sections considered in Fig. 7a are shown also in Fig. 7b. The velocity of the cooling fluid is about 3.36 m/s at the inlet (right hand side in Fig. 7), increases slightly where the flow section is reduced by the presence of the fin and reaches its maximum (about 22 m/s) where the cross section of the channel is at minimum. The local fluid velocity decreases significantly in the region between fins, especially in the corner like region at the base of the fin between the convergent/divergent part of the nozzle. The fluid is almost stagnant in these regions and possible problems due to reduced heat transfer efficiency may arise. Cooling fluid velocity increases again along the converging part of the nozzle (up to 20 m/s) and stabilizes at about 15 m/s along the combustion chamber. In this condition, the overall pressure drop along the cooling duct is about 1,500 Pa. The largest pressure gradient is observed along the convergent portion of the nozzle and above the combustion chamber. There, the cooling duct is narrow and the friction area between fluid and wall increases.

Results of the thermal calculations in the cooling fluid and in the solid shell are shown in Fig. 7c. Consider first the solid line, representing the temperature of the cooling fluid averaged over the channel thickness. The fluid flows from the right to the left, countercurrently to the expanding hot gas. The temperature of the cooling fluid increases from the inlet (480 K) to the outlet (600 K) of the cooling duct. Pre-heating calculated for the fluid is, on average, equal to $\Delta T = 120$ K. Heat recovery is rather effective to save energy on board, since the oxidizer can be pre-heated at no costs to reach the final temperature of
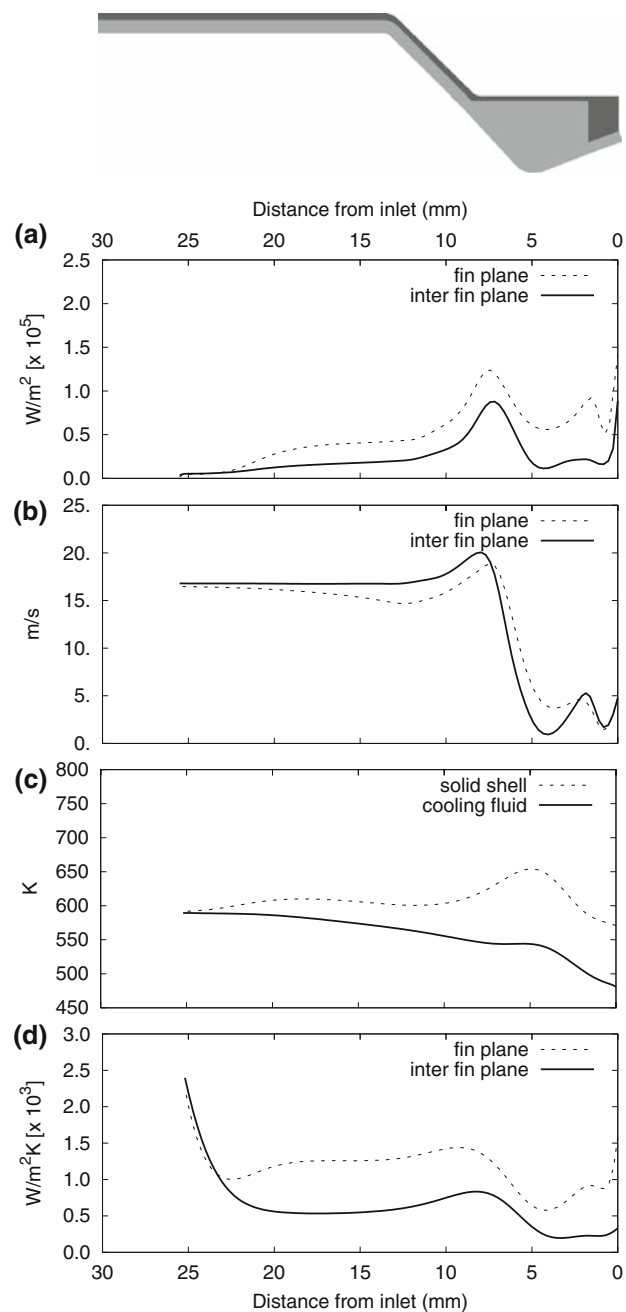
Fig. 7 Variation of quantities controlling heat transfer across the solid shell: **a** heat flux across the solid wall, **b** cooling fluid velocity, **c** solid and fluid temperature and **d** calculated local heat transfer coefficient along the cooling duct. *Dashed line* and *solid line* represent values calculated in the fin plane or in the inter fin plane in **a**, **b** and **d**, whereas represent values calculated in the solid shell and in the exhaust gases in **c**

injection in the combustion chamber. Consider now the dashed line, representing the variation of temperature in the solid shell, averaged across the shell thickness. The maximum temperature is found at the throat of the nozzle (660 K), where the heat flux is larger. The maximum local temperature in the shell is 811 K. This value is

sufficiently low to guarantee the mechanical and thermal resistance of the nozzle. Figure 7d shows the variation of the heat transfer coefficient on the cooling fluid side, calculated considering the heat flux transferred locally, $\dot{q}$, and the difference between the average temperature of the solid shell, T_{solid}, and that of the cooling fluid, T_{fluid}, at a given axial position:

$$H_c = \frac{\dot{q}}{T_{solid} - T_{fluid}}. \tag{5}$$

Variations of the heat transfer coefficient, H_c, are in the range 200–1,600 W/m^2 K in the nozzle region. The effect of the fins is to double the value of the local heat transfer coefficient with respect to the non finned portion of the cooling duct. In fact, this is crucial to guarantee the mechanical resistance of the solid shell. We calculated also the surface heat transfer coefficient, defined as the ratio between the local heat flux at the wall, $\dot{q}$, and the local temperature gradient at the surface. Variations of the surface heat transfer coefficient are in the range 1,600–8,000 W/m^2 K. The maximum value is found at the base of the fin and the minimum value at the tip of the fin. Average value of the surface heat transfer coefficient is $H_{ave} = 2,494$ W/m^2 K.

Even if the present design of the cooling system is found to be adequate to obtain effective cooling, the possibility to obtain the same effect using a simpler geometrical configuration was of interest to cut fabrication costs. We run a parallel simulation to verify if a simpler design of the cooling system, without fins to enhance the heat transfer from the wall of the nozzle to the cooling fluid, would perform satisfactorily. We found that, in this simplified configuration, the maximum temperature for the nozzle rises up to $T = 1,213$ K, i.e. it is more difficult to guarantee the mechanical resistance of the solid shell. Table 5 shows a comparison of performances for the two alternative configuration of the cooling system. Due to the specific shape of the cooling duct, characterized by a sink above the throat of the nozzle, the pressure drop increases slightly in the

configuration without fins, because the cooling fluid may recirculate in this region. In the configuration with fins, the increased resistance within each vane reduces this dissipative circulation. In the configuration without fins, the larger temperature of the solid determines also a higher peak value of temperature for the cooling fluid (about 1,190 K). This local increase in temperature does not correspond to a more effective pre-heating for the oxidizer, which is $\Delta T_{in,out} = 116$ K without fins and $\Delta T_{in,out} = 120$ K with fins. Variations are also observed in the homogeneity of temperature of the cooling fluid at the outlet section: $T_{out,fluid}$ is in the range 568–624 without fins and in the range 565–640 with fins. In the configuration with fins, hot spots of cooling fluid form at the fin tip and extend along the cooling duct without mixing significantly with the surrounding colder fluid. This is the reason why the temperature variation at the outlet ($\Delta T_{out,fluid}$) increases when fins are present. Overall, the heat transfer coefficient for the configuration without fins is $H_{ave} = 2,392.9$ W/m^2 K, i.e. only 5% less than the heat transfer coefficient for the configuration with fins. Yet, the variation of the local heat transfer in the most critical region guarantees larger safety margins for the mechanical resistance of the solid shell.

6 Conclusion

In this work, we exploit numerical simulations to examine alternative design configurations of a micro-rocket to be used for aerospace applications. Micro-rockets are complex system and the precise numerical analysis of the whole system would be costly and complex. The strategy proposed in this work, based on the hierarchical decomposition of the original problem into simpler problems, allows to identify sub-optimal design alternatives in short time and at low cost. The thrust of the micro-rocket is generated by the expansion of exhaust gases produced by a combustion process through a convergent/divergent nozzle.

Problem decomposition suggests that (1) the shape of the nozzle can be optimized to maximize the thrust neglecting the details of the gas combustion process occurring in the combustion chamber; (2) mixing of species and combustion process can be predicted correctly neglecting heat transfer from the combustion chamber if the reacting environment is properly confined; (3) heat transfer from the combustion chamber to solid boundaries can be included in the simulation only at the last stage, to verify if the micro-rocket cooling system is properly designed to prevent excessive over-heating of materials.

Results show that information obtained by "ad-hoc" designed numerical simulations can be sequentially improved to obtain a realistic evaluation of performances of the final apparatus. Experimental tests can then be focused

Table 5 Comparison of heat transfer performances for finned/no finned cooling duct configurations

	16 Fins	No fins
Δp (Pa)	1,500	1,620
$T_{max,solid}$ (K)	811	1,213
$T_{max,fluid}$ (K)	778	1,191
$\Delta T_{in,out}$ (K)	120	116
$T_{out,fluid}$ (K)	565–640	568–624
$\Delta T_{out,fluid}$ (K)	85	56
H_{local} (W/m^2 K)	1,600–8,000	1,960–7,500
H_{ave} (W/m^2 K)	2,494.5	2,392.9

on the reduced set of sub-optimal configurations identified by numerical simulations.

Appendix

Continuity, momentum and turbulence modeling

Conservation equations for mass, momentum and turbulent quantities solved by StarCD for general compressible flow in Cartesian notation are summarized in the following. Repeated subscripts denote summation.

Transport of mass

$$\frac{\partial \rho}{\partial t} + \frac{\partial}{\partial x_j}(\rho u_j) = s_m \tag{6}$$

where ρ is density, u_j are velocity components, t is time and s_m is the mass source.

Transport of momentum

$$\frac{\partial \rho u_i}{\partial t} + \frac{\partial}{\partial x_j}(\rho u_j u_i - \tau_{ij}) = -\frac{\partial p}{\partial x_i} + s_i \tag{7}$$

where p is the piezometric pressure, τ_{ij} are stress tensor components, s_i are momentum source components.

Transport of total enthalpy

$$\frac{\partial \rho H}{\partial t} + \frac{\partial}{\partial x_j}(\rho H u_j + F_{h,j} - u_i \tau_{ij}) = \frac{\partial p}{\partial t} + s_i u_i + s_h \tag{8}$$

where $H = u_i\, u_i/2 + h_t + \sum Y_m H_m$ is the total enthalpy and s_h is the energy source.

Transport of turbulent kinetic energy (RNG $k-\varepsilon$)

$$\frac{\partial}{\partial t}(\rho k) + \frac{\partial}{\partial x_j}\left(\rho u_j k - \left(\mu + \frac{\mu_t}{\sigma_k}\right)\frac{\partial k}{\partial x_j}\right)$$
$$= \mu_t(P + P_B) - \rho \varepsilon - \frac{2}{3}\left(\mu_t \frac{\partial u_i}{\partial x_j} + \rho k\right)\frac{\partial u_i}{\partial x_i} \tag{9}$$

where k is the turbulent kinetic energy, μ_t is the turbulent viscosity, σ_k is the turbulent Prandtl number, P and P_B are the rate of production of turbulent kinetic energy by the mean flow (incompressible and compressible contributions), $\rho\varepsilon$ is viscous dissipation and the last term represents the amplification/attenuation due to compressibility effects.

Transport of turbulence dissipation rate (RNG $k-\varepsilon$)

$$\frac{\partial}{\partial t}(\rho \varepsilon) + \frac{\partial}{\partial x_j}\left(\rho u_j \varepsilon - \left(\mu + \frac{\mu_t}{\sigma_\varepsilon}\right)\frac{\partial \varepsilon}{\partial x_j}\right)$$
$$= C_{\varepsilon_1}\frac{\varepsilon}{k}\left[\mu_t P - \frac{2}{3}\left(\mu_t \frac{\partial u_i}{\partial x_j} + \rho k\right)\frac{\partial u_i}{\partial x_i}\right]$$
$$+ C_{\varepsilon_3}\frac{\varepsilon}{k}\mu_t P_B - C_{\varepsilon_2}\rho\frac{\varepsilon^2}{k} + C_{\varepsilon_4}\rho\varepsilon\frac{\partial u_i}{\partial x_i}$$
$$- \frac{C_\mu \eta^3(1 - \eta/\eta_o)\rho\varepsilon^2}{1 + \beta\eta^3}\frac{}{k} \tag{10}$$

where σ_ε is the turbulent Prandtl number, $C_{\varepsilon_1}-C_{\varepsilon_4}$ are model coefficients, and the terms on the right-end side represent the contribution to the production of ε due to linear stresses and dilatation/compression effects, the contribution due to buoyancy, the destruction of ε, the contribution due to temporal mean density changes (of importance in combustion models), and the contribution due to non-linear stresses; the last term represents the effect of mean flow distortion on the turbulence with $\eta = Sk/\varepsilon$ and $S = (2\, S_{ij}S_{ij})^{1/2}$, S_{ij} being the mean strain tensor. All the constants of the model are given in Table 6.

Flow in the nozzle

Equations used to solve for the transitional flow inside the 2-D (and 3-D) nozzle are one mass (Eq. 6), two (three) momentum (Eq. 7) and one energy (Eq. 8) conservation equations. Slip boundary conditions are implemented through user defined subroutines as reported in Gad-el-Hak (1999).

Slip velocity at wall

$$u_g - u_w = \frac{2 - \sigma_v}{\sigma_v}Kn\left(\frac{\partial u}{\partial n}\right)_w + \frac{3\Delta T}{4\, T_o}\frac{1}{Re}\left(\frac{\partial T}{\partial s}\right)_w \tag{11}$$

where $Kn = \sqrt{\pi\gamma/2}Ma/Re$ is the Knudsen number, Re is the section averaged Reynolds number, n, s are the directions normal and parallel to the wall of the nozzle, γ is the specific heat ratio and σ_v is the accomodation factor for velocity.

Table 6 Coefficients of the RNG $k-\varepsilon$ turbulence model

C_μ	σ_k	σ_ε	C_{ε_1}	C_{ε_2}
0.085	0.719	0.719	1.42	1.68
	C_{ε_3}	C_{ε_4}	η_o	β
	0.0 or 1.42[a]	−0.387	4.38	0.012

[a] $C_{\varepsilon_3} = 1.42$ for $P_B > 0$ and 0 otherwise

Temperature jump at wall

$$T_g - T_w = \frac{2 - \sigma_T}{\sigma_T} \frac{2\gamma}{\gamma + 1} \frac{Kn}{Pr} \left(\frac{\partial T}{\partial n} \right)_w \qquad (12)$$

where σ_T is the accommodation coefficient for temperature and Pr is the Prandtl number.

Combustion modeling

Conservation equations solved by StarCD to simulate the chemical reaction using a presumed probability density function model for unpremixed reactions are summarized in the following. Repeated subscripts denote summation.

Transport of scalar species (solved for the leading reactant)

$$\frac{\partial \rho Y_m}{\partial t} + \frac{\partial}{\partial x_j}(\rho u_j Y_m + F_{m,j}) = s_m \qquad (13)$$

where Y_m is the mass fraction of component m, $F_{m,j}$ is the diffusional flux component, s_m is the rate of mass production/consumption for the component m.

Transport of the mean mixture fraction, $\overline{f}$

$$\frac{\partial \rho \overline{f}}{\partial t} + \frac{\partial}{\partial x_j}\left[\rho u_j \overline{f} - \left(\rho D_f + \frac{\mu_t}{\sigma_{f,t}}\right)\frac{\partial \overline{f}}{\partial x_j}\right] = S \qquad (14)$$

where $\sigma_{f,t}$ is the turbulent Schmidt number, D_f is the diffusion coefficient and S the source term (i.e. fuel from a different phase).

Transport of the variance of the mixture fraction, g_f

$$\begin{aligned}
\frac{\partial \rho g_f}{\partial t} + \frac{\partial}{\partial x_j}\left[\rho u_j g_f - \left(\rho D_g + \frac{\mu_t}{\sigma_g}\right)\frac{\partial g_f}{\partial x_j}\right] \\
= \frac{2\mu_t}{\sigma_g}\left(\frac{\partial \overline{f}}{\partial x_j}\right)^2 - C_D \rho \frac{\varepsilon}{k} g_f
\end{aligned} \qquad (15)$$

where the turbulent Schmidt number σ_g, and C_D have default values of 0.9 and 2, and $\overline{f}$ is the mean mixture fraction. Values of $\overline{f}$ and g_f are used to calculate the local value of f using the presumed form of the PDF distribution of f, which is a β function:

$$P(f) = \frac{f^{a-1}(1-f)^{b-1}}{\int_0^1 f^{a-1}(1-f)^{b-1}\,\mathrm{d}f} \qquad (16)$$

where $a = \overline{f}\left[\overline{f}(1-\overline{f}) - g_f\right]/g_f$ and $b = (1-\overline{f}) \cdot a/\overline{f}$. The mass fraction of any conserved scalar is given by:

$$\eta = f\eta_f + (1-f)\eta_o \qquad (17)$$

where η_f and η_o are the mass fractions of the scalar in the fuel stream and in the oxidizer.

Heat production and heat transfer

Chemico-thermal enthalpy balance

$$\begin{aligned}
\frac{\partial \rho h_t}{\partial t} + \frac{\partial}{\partial x_j}(\rho h_t u_j + F_{h_t,j}) = \frac{\partial p}{\partial t} + u_j \frac{\partial p}{\partial x_j} \\
+ \tau_{ij}\frac{\partial u_i}{\partial x_j} + s_h - \sum H_m s_{c,m}
\end{aligned} \qquad (18)$$

where h_t is the thermal enthalphy, $F_{ht,j}$ is the diffusional energy flux in direction x_j, s_h is the energy source, H_m and $s_{c,m}$ are the heat of formation and the rate of production/comsuption of species m due to chemical reaction.

Solid heat transfer

$$\frac{\partial \rho e}{\partial t} = \frac{\partial F_{e,j}}{\partial x_j} + s_e \qquad (19)$$

where $e = c_v T$ is the specific thermal energy of the solid, T is temperature, c_v is the specific heat and $F_{e,j}$ is the diffusional flux, given by

$$F_{e,j} = k\frac{\partial T}{\partial x_j} \qquad (20)$$

in the case of isotropic conductivity (k).

Boundary conditions used to solve the equations are given in the text of the paper.

References

Al-Abdeli YM, Masri AR (2003) Stability characteristics and flowfields of turbulent non-premixed swirling flames. Combust Theory Model 7:731–766

Battaglia F, Rehm RG, Baum HR (2000) The fluid mechanics of fire whirls: an inviscid model. Phys Fluids 12:2859–2867

Bayt R, Breuer K (2001) System design and performance of hot and cold supersonic microjets. AIAA-2001-0721. 39th AIAA Aerospace Sciences meeting and exhibit, Reno, Nevada, 8–11 January 2001

Bohn DE, Lepers J (2001) Numerical simulation of swirl-stabilized premixed flames with a turbulent combustion model based on a systematically reduced six-step reaction mechanism. J Eng Gas Turbines Power Trans ASME 123:832–838

Choudhuri AR, Baird B, Gollahalli SR, Schneider SJ (2000) Study of flow through microrocket nozzles. In: 12th Annual symposium on propulsion, propulsion engineering research center (PERC). Ohio Aerospace Institute, Cleveland, Ohio, 26–27 October 2000

Cuda S, Laundergan J, Sorenson E, Kessler B (1999) Computer software helps cut costs on delta series rockets. Air Space Eur 1:81–84

Eiamsa-ard S, Promvonge P (2007) Numerical investigation of the thermal separation in a Ranque-Hilsch vortex tube. Int J Heat Mass Transfer 50:821–832

Gad-el-Hak M (1999) The fluid mechanics of microdevices—the Freeman scholar lecture. J Fluids Eng 121:5–33

Hsu J, Mahalingam S (2003) Performance of reduced reaction mechanisms in unsteady non premixed flame simulations. Combust Theory Model 7:365–382

Huang RF, Tsai FC (2001) Flow field characteristics of swirling double concentric jets. Exp Thermal Fluid Sci 25:151–161

Hussaini MM, Korte JJ (1996) Investigation of low-Reynolds-number rocket nozzle design using PNS-based optimization procedure. NASA Technical Memorandum 110295, November 1996

Issa RI, Ahmadi Befrui B, Beshay K, Gosman AD (1991) Solution of the implicitly discretised reacting flow equations by operator-splitting. J Comp Phys 93:388–410

Jakirlic S, Jester-Zurker R, Tropea C (2004) Joint effects of geometry confinement and swirling inflow on turbulent mixing in model combustors: a second-moment closure study. Prog Comp Fluid Dyn 4:198–207

Ketsdever AD, Clabough MT, Gimelshein SF, Alexeenko A (2005) Experimental and numerical determination of micropropulsion device efficiencies at low Reynolds numbers. AIAA J 43:633–641

London AP, Epstein AH, Kerrebrock JL (2001) High pressure bipropellant microrocket engine. J Propuls Power 17:780–787

Marinov NM (1999) A detailed chemical kinetic model for high temperature ethanol oxydation. Int J Chem Kinet 31:183–220

Miotti P, Tajmar M, Guraya C, Perennes F, Marmiroli B, Soldati A, Campolo M, Kappenstein C, Brahmi R, Lang M (2004) Bi-propellant micro-rocket engine. AIAA 2004-6707. CANEUS 2004 conference on micro-nano-technologies, Monterey, California, 1–5 November 2004

Park TW, Katta VR, Aggarwal SK (1998) On the dynamics of a two-phase, non evaporating swirling flow. Int J Multiphase Flow 24:295–317

Patankar SV, Spalding DB (1972) A calculation procedure for heat and mass transfer in three dimensional parabolic flows. Int J Heat Mass Transfer 15:1787–1806

Reed BD (2004) On-board chemical propulsion technology. NASA/TM-2004-212698, prepared for 10th international workshop on combustion and propulsion, La Spezia, Italy, 21–25 September 2003

Richardson JM, Howard Jr, HC, Smith RW (1953) The relation between sampling tube measurements and concentration fluctuations in a turbulent gas jet. In: 4th Symposium on combustion, pp 814–817

Rossi C, Orieux S, Larangot B, Do Conto T, Esteve D (2002) Design, fabrication and modeling of solid propellant microrocket-application to micropropulsion. Sensor Actuators A 99:125–133

Rouse WB (2003) Engineering complex systems: implications for research in systems engineering. IEEE Trans Syst Man Cybern C Appl Rev 33:154–156

Sankaran V, Menon S (2002) LES of spray combustion in swirling flows. J Turbul 3:11–21

Scharlemann C, Schiebl M, Marhold K, Tajmar M, Miotti P, Kappenstein C, Batonneau Y, Brahmi R, Hunter C (2006) Development and test of a miniature hydrogen peroxide monopropellant thruster. AIAA-2006-4550. AIAA joint propulsion conference, Sacramento, California, 9–12 July 2006

Schley CA, Hagemann G, Krülle G (1997) Towards an optimal concept for numerical codes simulating thrust chamber processes in high pressure chemical propulsion systems. Aerospace Sci Technol 3:203–213

Snegirev AY, Marsden JA, Francis J, Makhviladze GM (2004) Numerical studies and experimental observations of whirling flames. Int J Heat Mass Transfer 47:2523–2539

Yakhot V, Orszag SA (1986) Renormalization group analysis of turbulence. J Sci Comput 1:3–20

Zhou X, Sun Z, Durst F, Brenner G (1999) Numerical simulation of turbulent jet flow and combustion. Comput Math Appl 38:179–191